Colossal Ultraviolet Photoresponsivity of Few-Layer Black Phosphorus

Jing Wu,[†,‡,§,#] Gavin Kok Wai Koon,[†,‡,§,#] Du Xiang,[†,‡,#] Cheng Han,[†,‡] Chee Tat Toh,[†,‡] Eeshan S. Kulkarni,[†,‡] Ivan Verzhbitskiy,[†,‡,∥] Alexandra Carvalho,[†,‡] Aleksandr S. Rodin,[‡] Steven P. Koenig,[†,‡] Goki Eda,[†,‡,∥] Wei Chen,[†,‡,∥,⊥] A. H. Castro Neto,[†,‡] and Barbaros Özyilmaz*[,†,‡,§]

[†]Department of Physics, [‡]Centre for Advanced 2D Materials and Graphene Research Centre, and [∥]Department of Chemistry, National University of Singapore, 117542, Singapore, [§]NanoCore, National University of Singapore, 117576, Singapore, and [⊥]National University of Singapore (Suzhou) Research Institute, 377 Lin Quan Street, Suzhou Industrial Park, Jiang Su 215123, China. [#]J.W., G.K.W.K., and D.X. contributed equally.

ABSTRACT Black phosphorus has an orthorhombic layered structure with a layer-dependent direct band gap from monolayer to bulk, making this material an emerging material for photodetection. Inspired by this and the recent excitement over this material, we studied the optoelectronics characteristics of high-quality, few-layer black phosphorus-based photodetectors over a wide spectrum ranging from near-ultraviolet (UV) to near-infrared (NIR). It is demonstrated for the first time that black phosphorus can be configured as an excellent UV photodetector with a specific detectivity $\sim 3 \times 10^{13}$ Jones. More critically, we found that the UV photoresponsivity can be significantly enhanced to $\sim 9 \times 10^4$ A W^{-1} by applying a source-drain bias (V_{SD}) of 3 V, which is the highest ever measured in any 2D material and 10^7 times higher than the previously reported value for black phosphorus. We attribute such a colossal UV photoresponsivity to the resonant-interband transition between two specially nested valence and conduction bands. These nested bands provide an unusually high density of states for highly efficient UV absorption due to the singularity of their nature.

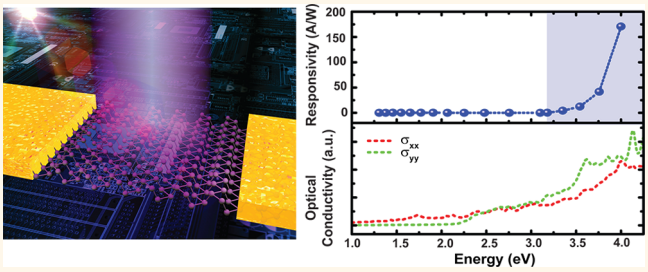

KEYWORDS: black phosphorus · direct band gap · ultraviolet · optoelectronics · phototransistor

Black phosphorus has a layered crystal structure enabling mechanical exfoliation of bulk crystals into thin films.[1,2] However, black phosphorus exhibits a highly anisotropic crystal structure unlike other 2D materials, causing its optical and electronic properties to be direction dependent.[2−5] The phosphorus atoms within the layers are bonded covalently to three neighboring atoms forming a puckered orthorhombic lattice,[6,7] and each phosphorus atom has five valence electrons. This makes black phosphorus a layer-dependent direct band gap semiconductor[7,9,10] with the energy gaps predicted to increase from ∼0.3 eV for bulk to 2 eV for single layer,[8] which differentiates black phosphorus from most of the transition-metal dichalcogenides (TMDs)[9] where direct band gap is only possible for monolayer.[10] TMDs have recently attracted intensive interest in optoelectronics attributed to the strong light absorption leveraged on the presence of direct band gap. In addition to the intrinsic direct band gap, the relatively small gap of multilayers allows black phosphorus to be tuned easily from the OFF to ON conductance state.[11] The reasonably high hole mobility, 100−1000 cm^2 V^{-1} s^{-1}, and current modulation ∼10^5 of thin black phosphorus FETs make the material suitable for not only transistor applications but also for optoelectronics devices.[1−3,11−14]

Black phosphorus can be seen as a crystal generated by periodic repetition of tetraphosphorus (P_4) molecules.[15] It is known that tetraphosphorus P_4 can be transformed temporarily to diphosphorus P_2 upon ultraviolet (UV) irradiation,[16,17] which is often desirable because the latter form has a highly reactive π bond for many chemistry applications.[18−20] Thus, it is expected that the P_4-structured black phosphorus also has strong interactions with illumination, especially UV light.[16,17] Indeed, a black phosphorus based photodetector has been shown to have responsivity of 4.8 mA W^{-1} in the visible light regime,[21] and its potential for fast imaging applications has also been

* Address correspondence to phyob@nus.edu.sg.

Received for review March 31, 2015 and accepted July 24, 2015.

Published online July 24, 2015
10.1021/acsnano.5b01922

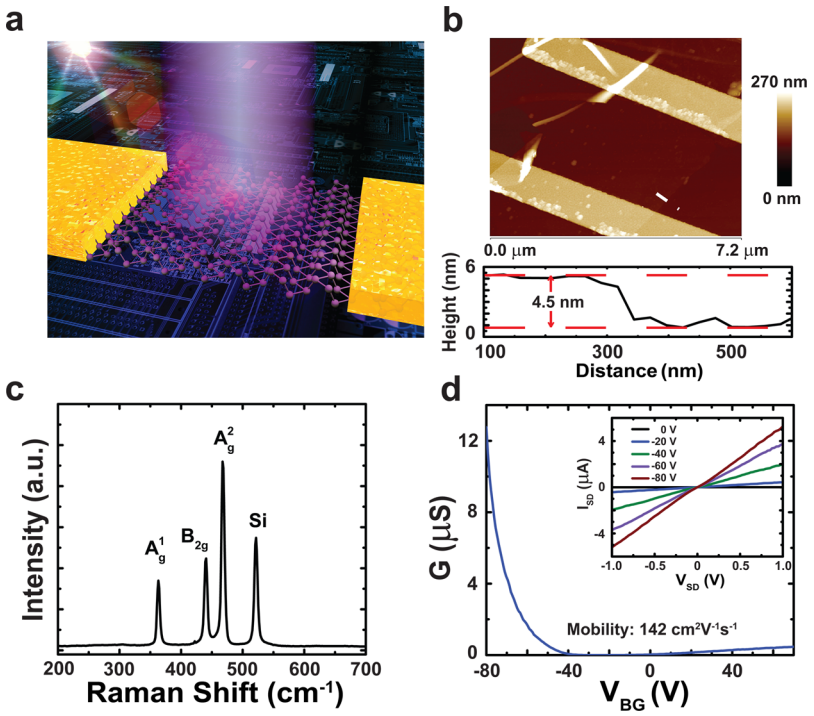

Figure 1. Few-layer black phosphorus photo-FET and characterizations. (a) Three-dimensional view of the device structure used to measure photoresponse. (b) AFM scan across the channel area of our device showing the thickness of the black phosphorus flake to be ~4.5 nm. (c) Raman analysis on the black phosphorus flake used to make photo-FET. (d) Conductance as a function of back gate voltage with V_{SD} = 0.1 V. Inset: $I-V$ characteristics of the same junction with different applied back gate voltages.

demonstrated in both the visible light and near-infrared regime.[12] Moreover, recent study reports an even higher responsivity (~10^2mA/W) of black phosphorus based phototransistor in the visible light regime[22] through contact-engineering. However, optoelectronic characterization of this material in the near UV range is still absent. UV detection is of great technological interest, and the need for applications ranges from simple fire detector, chemical markers, and forensics studies to detectors positioned in space for niche astronomical observations.[23]

Here, we used black phosphorus as our semiconducting channel in photo-FETs. Upon illumination, light will be converted directly into current in our phototransistor. We demonstrate for the first time a wide range photocurrent response of black phosphorus photo-FETs, from 310 to 950 nm (from near UV to visible light-NIR), in our devices. In our photocurrent measurements, two distinct photoelectric behaviors were discovered, and we conducted them in two different regimes due to the transition dependence of energy: the low energy range, from 1.3 to 3.1 eV, and the high energy range, from 3.2 to 4 eV. We obtained highest photoresponsivity of 9×10^4 A W^{-1} in the near-UV regime (high energy range) and ~1.82 A W^{-1} in the visible light-NIR regime (low energy range). The photo responsivity of black phosphorus devices in the near UV regime is 5 orders of magnitude higher than in the visible light-near-infrared regime. Our measurement translates into a specific detectivity of $\sim 3 \times 10^{13}$ Jones comparable to other UV detectors (see the Supporting Information, Table 1). Together with a reasonable mobility of ~142 cm^2 V^{-1} s^{-1} and ON-current of ~0.1−1 μA, black phosphorus indeed shows a vast potential for practical applications in optoelectronic devices.

RESULTS AND DISCUSSION

A schematic diagram for our photo FET is illustrated in Figure 1a, and Figure 1b shows the AFM scan of a black phosphorus photo FET device with two metal contacts. The line profile presents the typical height of the crystal used in making the devices ~4.5 nm. The first-order Raman spectrum of few-layered black phosphorus on silicon substrate, as shown in Figure 1c, demonstrates several prominent peaks around ~360, 440, 470, and 520 cm^{-1}. The latter peak corresponds to the silicon substrate, while the first three originate from the vibrational modes of black phosphorus crystal lattice, namely A^1_g, B_{2g}, and A^2_g, respectively.[24]

All electronic measurements were performed with a two-terminal DC technique under room temperature and high vacuum conditions (~10^{-7} mbar). We first characterized these devices by measuring the back gate dependence of the conductance (Figure 1d). Our devices show transistor ON/OFF in the orders of 10^5 as we tuned the back gate voltage. From the

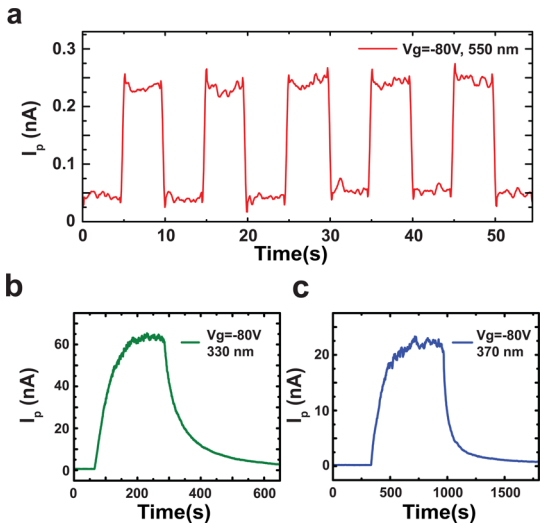

Figure 2. Time dependence of photocurrent of few-layer black phosphorus-based FET in two different wavelength regimes. (a) Fast response of photocurrent induced by excitation of 550 nm light source at $V_{BG} = -80$ V. (b, c) Slow response of photocurrent at high energy regime under wavelength 330 and 370 nm.

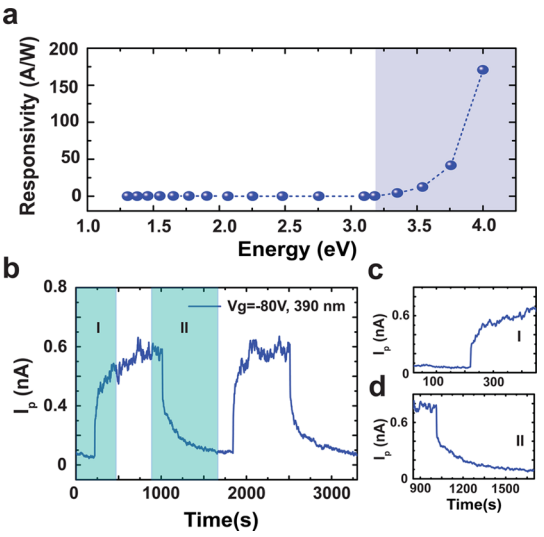

Figure 3. Photoresponsivity of few-layer black phosphorus phototransistor. (a) Photoresponsivity of our device within the energy range 1−4 eV measured at $V_{BG} = -80$ V and $V_{SD} = 0.1$ V. (b) Combination of fast and slow response of photocurrent with excitation of 390 nm light source at the same applied back gate. Region I shows the sharp increase followed by gradual increase of photocurrent while the light source is turned ON. Similarly, in region II, there is a sudden drop followed by gradual decrease of photocurrent when the light is turned OFF. (c) Zoom in plot of region I as shown in (b). (d) Similar to that for for region II.

transconductance measurements, we can extract the field effect mobility based on the equation[25]

$$\mu = \frac{L}{WC}\frac{dG}{dV_{BG}}$$

where L and W are the length and width of our device channel and C is the capacitance per unit area. We obtain field effect hole mobility of ~142 $cm^2 V^{-1} s^{-1}$ comparable to previous works on thin black phosphorus.[1−3,11] Figure 1d (inset) shows the $I-V$ characteristics of the two contacts with different applied gate bias (V_{BG}).

To study the photoresponse of our FETs, we used a monochromatic xenon light source with tunable wavelengths (310−950 nm) and power density (2−31 mW cm^{-2}).[26,27] Unlike photodiodes that can extract charge carriers from electron−hole pairs by the PN junction, a bias voltage is required to induce the current for the phototransistor. In Figure 2a we show time-dependent photoresponse at the ON state of our device ($V_{BG} = -80$ V) upon illumination of 550 nm wavelength light source (see the Supporting Information, Figures S1 and S3, for other excitation wavelengths). In the low energy range, we observe a fast photocurrent response time in the order of milliseconds (ms). As shown in Figure S2, the rise time of the photocurrent is ~1 ms, and the fall time is ~4 ms. If we increased the energy of the light source by decreasing the wavelength to near UV range, a photoresponse which shows a totally different behavior is observed. Parts b and c of Figure 2 show the photocurrent under the wavelength 330 and 370 nm. Comparing these two parts with Figure 2a, we can find that unlike the sudden jump in photocurrent at the low energy regime, a gradual increase started after the illumination treatment on the sample. The photocurrent later shows saturation after ~200s, which yields a much longer response time than the low energy regime. Such a long response time is comparable to that for other UV photodetectors.[28,29] However, the photocurrent increased by 2 orders of magnitude in this slow photoresponse. In the low energy range, the fast response time can be ascribed to the conventional photon absorption with the excited electron hole pairs undergoing band-to-band recombination. We believe that the long response time that we observe for high energy excitation (near UV) is due to recombination of electron−hole pairs through trap centers coming from defects or charge impurities.[30] This is consistent with the fact that black phosphorus degrades quickly in ambient to form layers of oxides/charged impurities from air.[1]

The photoresponsivity (PR) and external photogain of our device in two different wavelength ranges, namely in the ranges 400−950 and 310−390 nm, were calculated from the previous photocurrent measurements (Figure 3a). For a typical photodetector, the photoresponsivity is defined as response current created by a unit power of excitation light on the effective area of the photo detector

$$(\mathrm{PR}) = \frac{\Delta I}{PA_S}$$

where ΔI is the excited photocurrent, P is the intensity of the light power, and A_S is the effective area of our

channel. Meanwhile, the external photogain can be computed *via* the following equation[30,31]

$$\text{externalgain} = \frac{\Delta I}{e \times \Delta n \times A_S}$$

where Δn is the number of excited electron hole pairs and e is the electron charge. In this photoconductor configuration, the external photogain can be as high as $\sim 10^6$ (see the Supporting Information). In the fast response time range, the photoresponsivity shows a maximum of $\sim$90 mA W^{-1} at wavelength of 800 nm. On the other hand, in the slow response time range, a clear increase of photoresponsivity can be observed while the wavelength of the light sources decreased from 390 to 310 nm with a maximum photoresponsivity as high as 175 A W^{-1}. We plotted the time-dependent photocurrent curve under the transition wavelength between the fast and slow response in Figure 3b. From the blown up plots for the increasing region I (Figure 3c) and the decreasing region II (Figure 3d), we can find that the two distinct steps actually both contribute to the photocurrent. When the light was on, the excited carriers traveled for milliseconds and then recombined back to the valence band, which induced the fast photocurrent in the sample. As the energy of the photons in the light source increased, more carriers from the lower valence band were excited and jumped to the upper conduction band after absorption of high energy photons, which can be also elucidated by our later theoretical calculation. This provided a large amount excited carriers and made excited carriers much more difficult to recombine back to the valence band. The excited carriers circulated in the external for circuit many times[32] before recombination with their trapped counterparts.[33] The circulation of the photogenerated carriers contributed to the photocurrent leading to large photoresponsivity and long response time.[28,29] As the energy increased, the contribution from the slow response increased with the number of circulation, and it is much larger than the fast response. From Figure 2b,c, the contribution of fast response was screened by the slow response. All of the measurements were carried out under a source drain bias of 0.1 V and gate bias of −80 V. Another central figure of merit often used to compare the performance of photodetectors is the specific detectivity[34]

$$D = \frac{(\text{PR})\sqrt{A_S f}}{S_N}$$

where f is the frequency bandwidth and S_N is the noise spectral density. In our case, the specific detectivity amounts to be $\sim 3 \times 10^{13}$ Jones, which is in the order of the current state of the art UV detectors.[34]

For better understanding of the energy-dependent photoresponsivity, a theoretical curve for the optical conductivity σ is shown in Figure 4a, obtained by

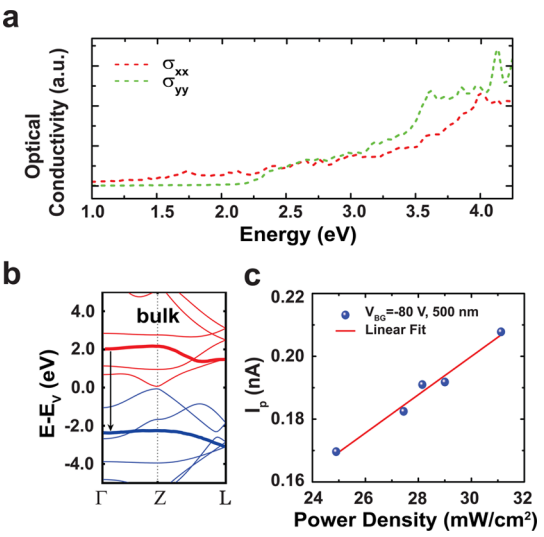

Figure 4. Theory calculation of black phosphorus. (a) Theoretical optical conductivity, obtained from first principles. (b) Black phosphorus band structure, obtained from first-principles calculations. The arrow indicates the band nesting responsible for the earliest absorption edge in the UV (between 3 and 4 eV). (c) Photocurrent as a function of power density measured at $V_{BG} = -80$ V, $V_{SD} = 0.1$ V, and a fixed light source of 500 nm.

adopting an independent electron approximation within the density functional theory framework. The measured photoconductivity has contributions both from the σ_{xx} and σ_{yy} components of the optical conductivity tensor. As in experiment, σ_{xx} has a first absorption edge at the gap energy (positioned at 0.1 eV in the theoretical curve), but the largest absorption actually happens in the UV range. Between 3 and 4 eV, there is a group of high peaks on both σ_{xx} and σ_{yy} The dominant high absorption peaks originate on the nested valence and conduction bands are nearly flat between Gamma and Z, indicated by an arrow in Figure 4b. This is similar to the band-nesting in semiconducting transition-metal dichalcogenides.[35] The fact that the peak energies do not coincide exactly with experiment is due to two sources of error in the theoretical working approximations, which partially cancel: a systematic underestimation of the energy of the conduction bands, arising from the discontinuity of the exchange-correlation energy, and ignoring the exciton binding energy, which would shift the absorption peaks toward higher energies. According to a recent GW study, these shifts are about 1.2 and 0.8 eV, respectively.[8] In addition to the photoresponsivity measurements, we have also conducted experiments to obtain the absorption spectrum of few-layer black phosphorus by first measuring the differential reflectance. The fact that we observe a high differential reflectance in the near UV energy range provides a strong argument for the high activity of black phosphorus at larger energies (see the Supporting Information, Figure S4).

To further confirm the photocurrent generation in our device, we study the power density dependence of

the photocurrent at a fixed wavelength of 500 nm. As shown in Figure 4c, the photocurrent varies linearly with the intensity of the light power (25−31 mW cm^{-2}) as expected from the second equation above. From the linear fit of the plot, we can extract the gradient of the line 6.1 nA cm^2 W^{-1} which agrees well with our measurements (PR)A_S = 6.3 nA cm^2 W^{-1}.

In Figure 5, we investigate the source drain bias V_{SD} dependence of the photoresponsivity of our device. As before, we separate the results into two different regimes; visible light−NIR and near-UV regimes. Figure 5a shows the V_{SD} dependence of the responsivity for low energy range excitation (500 nm). We observed a linear increase in responsivity from ∼50 to ∼1.82 A W^{-1} as we increase the V_{SD} from 0.1 to 3 V. A similar response was seen in the near UV excitation whereby the responsivity increased up to ∼9 × 10^4 A W^{-1} for V_{SD} = 3 V (Figure 5b). In addition, its source drain bias-dependent photoresponse is comparable to that reported previously.[13]

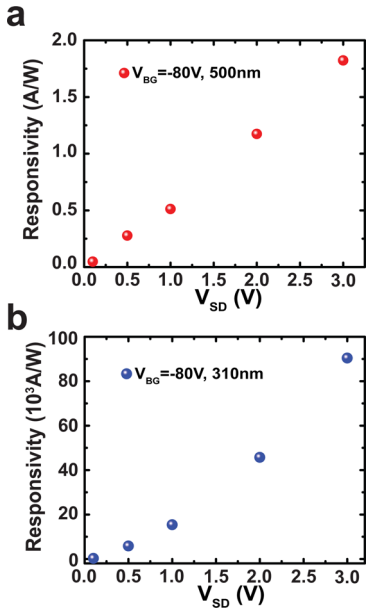

Figure 5. Source drain voltage dependence of photoresponsivity. (a) Photoresponsivity in the low energy excitation range (visible light−IR) measured at V_{BG} = −80 V. (b) Photoresponsivity in the high energy excitation range (near-UV) measured at V_{BG} = −80 V.

We now analyze the relation between the photoconductivity and the orientation of the sample relative to the light polarization. First, we use Raman measurements (Figure 6a) to establish the orientation of the crystal axes relative to the device terminals. From the first-principles calculations of the Raman tensor, we find that the intensity of the A^1g and A^2g modes is much lower along the direction of the black phosphorus zigzag ridges (*y*) than along the perpendicular direction (*x*). In fact, the ratio between the R_{xx} and R_{yy} components of the Raman tensor is R_{xx}/R_{yy} = 300 for the A^2g mode and 140 for the A^1g mode. Thus, from the dependence of the Raman intensity of the A^2g mode on the polarization angle, we deduce that the SD direction is oriented along the *y*-axis of the crystal.

Further, we expect to see a change in photocurrent as we vary the polarization angle due to the anisotropic crystal structure of black phosphorus crystals.[3,36] This is clearly seen in Figure 6b. The photocurrent shows 180° rotational symmetry, with minima at 0° and 180° (when the polarization of the incident light electric field is perpendicular to the SD direction) and maxima at 90° and 270° (when the polarization of the incident light electric field is parallel to the SD direction). This angular dependence can be related to the anisotropy of the σ tensor by assuming that the current density along the y direction (j_y) is given by $j_y = t(\theta)\sigma_{yy}E_y \sin\theta$, where E_y is the *y* component of the incident electric field and *t* is the ratio between the magnitudes of the transmitted and incident electric fields, given by

$$t(\theta)^2 = 4\cos(\theta)^2/(1+n+4\pi\sigma_{xx}\mu_0/c)^2 + 4\sin(\theta)^2/(1+n+4\pi\sigma_{yy}\mu_0/c)^2$$

where *n* is the refraction index, *c* is the speed of light, and μ_0 is the vacuum permeability. Here, we assume that the dielectric constant is approximately isotropic and that the incident and transmitted polarization angles are approximately the same. If the generated

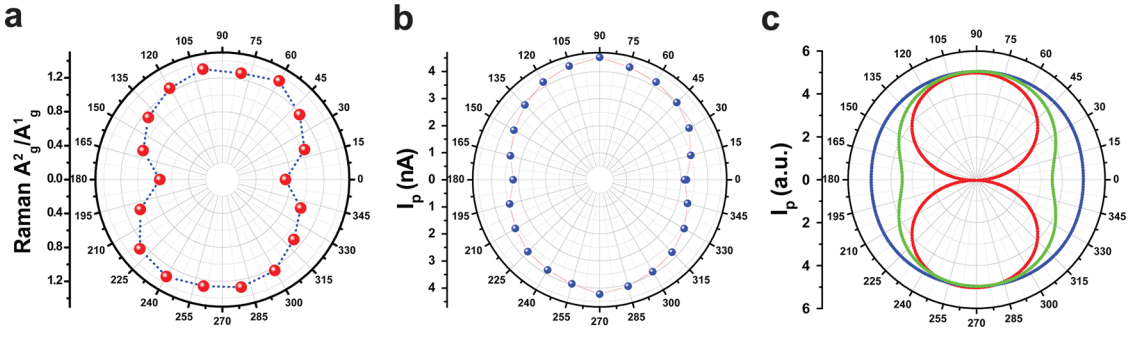

Figure 6. Photocurrent dependence on the polarized light angle. (a) Measured polarization dependence of the intensity of the A^2g/A^1g Raman peak. (b) Photocurrent measured with laser source of 405 nm wavelength at different light polarization angle with V_{SD} = 0.1 V and V_{BG} = −80 V, showing a 180° rotational symmetry. (c) Simulated dependence of the photocurrent on the light polarization angle, for $j^2 = aj_x^2 + j_y^2$, where *a* is the collection efficiency for currents perpendicular to the DC field for *a* = 0 (red), *a* = 0.5 (green), and *a* = 1 (blue).

current density is collected independently of its polarization, the polarization dependence is given by an ellipsoid (Figure 6c); however, because electron−hole pairs are more efficiently separated and collected when j is parallel to the DC field, the shape of the curve is slightly narrower along the *x* (horizontal) axis, which is perpendicular to the SD direction.

Last, we note that the electron and hole lifetimes, which limit the photoresponsivity, are predominantly determined by the type of defects present. Due to the reactivity of the surface of black phosphorus,[1] high concentration of impurities aggregates on the surface and majority of these are oxygen impurities. According to a recent study, oxygen point defects and aggregates are normally electrically inactive, except for surface metastable bridging oxygen, which may introduce both donor and acceptor states.[37] Such oxygen impurities are unavoidable as long as the exfoliations of these flakes and the subsequent device fabrication are not performed in an inert environment (glovebox). Hence, the performance of BP-based UV detectors are likely to increase by encapsulating[38] it with, *e.g.*, Al_2O_3, to protect the top layer from degradation.[39] Combining black phosphorus with graphene instead and forming a van der Waals heterostructure is also a potential way to improve the performance of black phosphorus based UV photodetector.[40,41] In such devices, the internal potential difference can help by separating the electrons and holes quickly. The high carrier mobility of graphene should allow for a much shorter response time. Using a BN substrate can also reduce the impact of interface traps such as Si dangling bonds at the SiO_2 surface and hence can also reduce recombination centers. Besides controlling the concentration of impurities, Lopez-Sanchez *et al.* have demonstrated a gate pulse method which can reduce the decay time by discharge of the trapped charge carriers.[9] Interface traps such as Si dangling bonds at the SiO_2 surface also provide recombination centers. These are similar to the E′ centers[42,43] and have acceptor levels between 2 and 4 eV below the conduction band of SiO_2, with some therefore resonating with the conduction band states and behaving as efficient electron traps (see Figure S5, Supporting Information).

CONCLUSION

To summarize, we have shown the potential of black phosphorus to be used as a photodetector material with a wide electromagnetic range of photocurrent response. We showed photoresponse in black phosphorus FETs with a reasonable field effect mobility and high ON/OFF current modulation. We identify two distinct mechanisms for the photocurrent response at two different energy ranges. Because of the intrinsic direct band gap of black phosphorus, we obtain a maximum photoresponsivity of $\sim 9 \times 10^4$ A W^{-1}, and the calculated external photogain can be as high as 10^8. The measured responsivity is several orders of magnitude higher compared to other 2D materials.[9] We believe the colossal photoresponsivity is due to band nesting and corresponding singularity in the join density of states. To provide a more direct comparison with other photodetectors, we have calculated the specific detectivity of our device to be $\sim 3 \times 10^{13}$ Jones in the near UV spectrum. Moreover, the existence of this small direct band gap allows black phosphorus to be continuously tuned from the ON to OFF state of this transistor. Black phosphorus proved to be a strong viable candidate for future optoelectronic applications especially as state of the art UV detectors.

METHODS

Sample Fabrication. For the first step of our device fabrications, we used micromechanical exfoliation method to obtain few layers black phosphorus (Smart Elements) on p-doped silicon wafers with 300 nm SiO_2. The wafers have been previously treated with O_2 plasma to clean and activate the surface. Immediately after locating the few-layer flake of black phosphorus based on the optical contrast and Raman measurements, we spin-coated electron beam resist poly(methyl methacrylate) PMMA to protect the flake because of its fast degradation in ambient.[1,44] Next, we employed electron beam lithography to pattern electrodes and thermal metal evaporation for deposition of 5/80 nm thick Ti/Au contacts.

Measurement Setup. All electronic measurements were performed at room temperature and under high vacuum condition $\sim 10^{-7}$ mbar.[26,27] DC electrical measurements were performed using Agilent B2912A. The light source used throughout the experiments was supplied by a monochromatic xenon light source with tunable wavelengths. For the polarization measurements, the excitation source is supplied by laser source with wavelength of 405 nm.

The Raman spectra were recorded with Witec Confocal Raman setup equipped with 532 nm laser line and spectral resolution 2−3 cm^{-1}. The polarization map was obtained with a fixed laser and scattered light polarizations (parallel to each other), while the half-wave plate was placed between the sample and the beam splitter varying the polarization of the incident light. The scattered light was collected by 50× long-distance objective.

Theory Calculation. First-principles calculations based on density-functional theory were used to compute the electronic structure of black phosphorus. The bulk crystal was used as a model. The calculations were performed using the Quantum ESPRESSO code[45] and postprocessed using a modified version of the epsilon code. The core electrons were treated using the projector augmented wave method.[46] The exchange correlation energy was described by the generalized gradient approximation (GGA) using the PBE functional,[47] except for the Raman tensor, which was calculated using the local density approximation.[48] The Kohn−Sham orbitals were expanded in a plane-wave basis with a cutoff energy of ~70 Ry. The charge density was calculated using 8 × 8 × 6 points of the Brillouin zone, following the scheme proposed by Monkhorst−Pack,[49] whereas the optical conductivity was calculated by sampling the band structure in a mesh of 30 × 30 × 10 points of the reciprocal space. The Raman tensors were calculated using the perturbative method outlined in ref 46.[50]

Conflict of Interest: The authors declare no competing financial interest.

Supporting Information Available: The Supporting Information is available free of charge on the ACS Publications website at DOI: 10.1021/acsnano.5b01922.

Details on the sample fabrication, measurement setups, theory for simulation, and additional data with discussion (PDF)

Acknowledgment. We thank Ivan J. Vera-Marun and Zhao Weijie for helpful discussions and comments. B.Ö. acknowledges support by the National Research Foundation, Prime Minister's Office, Singapore, under its Competitive Research Programme (CRP Award No. NRF-CRP9-2011-3) and Research Fellowship (RF Award No. NRF-RF2008-7), and the SMF-NUS Research Horizons Award 2009-Phase II. A.H.C.N. acknowledges support by the National Research Foundation, Prime Minister's Office, Singapore, under its Competitive Research Programme (CRP Award No. NRF-CRP6-2010-5). The calculations were performed in the GRC computing facilities. W.C. acknowledges the support from Singapore MOE Grant No. R143-000−559-112. G.E acknowledges the Singapore National Research Foundation for funding the research under NRF Research Fellowship (NRF-NRFF2011-02). B.Ö. supervised the project. J.W. and B.O. designed the experiments. J.W. and X.D. performed the experiments. A.C. carried out the theory calculation. G.K., W.K., and J.W. wrote the manuscript. All authors carried out the data analysis and discussed the results.

REFERENCES AND NOTES

1. Koenig, S. P.; Doganov, R. A.; Schmidt, H.; Castro Neto, A. H.; Özyilmaz, B. Electric Field Effect in Ultrathin Black Phosphorus. *Appl. Phys. Lett.* **2014**, *104*, 103106.
2. Liu, H.; Neal, A. T.; Zhu, Z.; Luo, Z.; Xu, X.; Tománek, D.; Ye, P. D. Phosphorene: An Unexplored 2D Semiconductor with a High Hole Mobility. *ACS Nano* **2014**, *8*, 4033–4041.
3. Xia, F.; Wang, H.; Jia, Y. Rediscovering Black Phosphorus as An Anisotropic Layered Material for Optoelectronics and Electronics. *Nat. Commun.* **2014**, *5*.10.1038/ncomms5458
4. Liu, H.; Du, Y.; Deng, Y.; Ye, P. D. Semiconducting Black Phosphorus: Synthesis, Transport Properties and Electronic Applications. *Chem. Soc. Rev.* **2015**, *44*, 2732–2743.
5. Ling, X.; Wang, H.; Huang, S.; Xia, F.; Dresselhaus, M. S. The Renaissance of Black Phosphorus. *Proc. Natl. Acad. Sci. U. S. A.* **2015**, *112*, 4523–4530.
6. Zhang, C. D.; Lian, J. C.; Yi, W.; Jiang, Y. H.; Liu, L. W.; Hu, H.; Xiao, W. D.; Du, S. X.; Sun, L. L.; Gao, H. J. Surface Structures of Black Phosphorus Investigated with Scanning Tunneling Microscopy. *J. Phys. Chem. C* **2009**, *113*, 18823–18826.
7. Brown, A.; Rundqvist, S. Refinement of The Crystal Structure of Black Phosphorus. *Acta Crystallogr.* **1965**, *19*, 684–685.
8. Tran, V.; Soklaski, R.; Liang, Y.; Yang, L. Layer-Controlled Band Gap and Anisotropic Excitons in Few-Layer Black Phosphorus. *Phys. Rev. B: Condens. Matter Mater. Phys.* **2014**, *89*, 235319.
9. Lopez-Sanchez, O.; Lembke, D.; Kayci, M.; Radenovic, A.; Kis, A. Ultrasensitive Photodetectors Based on Monolayer MoS_2. *Nat. Nanotechnol.* **2013**, *8*, 497–501.
10. Morita, A. Semiconducting Black Phosphorus. *Appl. Phys. A: Solids Surf.* **1986**, *39*, 227–242.
11. Li, L.; Yu, Y.; Ye, G. J.; Ge, Q.; Ou, X.; Wu, H.; Feng, D.; Chen, X. H.; Zhang, Y. Black Phosphorus Field-Effect Transistors. *Nat. Nanotechnol.* **2014**, *9*, 372–377.
12. Engel, M.; Steiner, M.; Avouris, P. Black Phosphorus Photodetector for Multispectral, High-Resolution Imaging. *Nano Lett.* **2014**, *14*, 6414–6417.
13. Youngblood, N.; Chen, C.; Koester, S. J.; Li, M. Waveguide-Integrated Black Phosphorus Photodetector with High Responsivity and Low Dark Current. *Nat. Photonics* **2015**, *9*, 247–252.
14. Deng, Y.; Luo, Z.; Conrad, N. J.; Liu, H.; Gong, Y.; Najmaei, S.; Ajayan, P. M.; Lou, J.; Xu, X.; Ye, P. D. Black Phosphorus−Monolayer MoS_2 van der Waals Heterojunction p−n Diode. *ACS Nano* **2014**, *8*, 8292–8299.
15. Pauling, L.; Simonetta, M. Bond Orbitals and Bond Energy in Elementary Phosphorus. *J. Chem. Phys.* **1952**, *20*, 29–34.
16. Rathenau, G. Optische Und Photochemische Versuche Mit Phosphor. *Physica* **1937**, *4*, 503–514.
17. Piro, N. A.; Figueroa, J. S.; McKellar, J. T.; Cummins, C. C. Triple-Bond Reactivity of Diphosphorus Molecules. *Science* **2006**, *313*, 1276–1279.
18. Back, O.; Kuchenbeiser, G.; Donnadieu, B.; Bertrand, G. Nonmetal-Mediated Fragmentation of P4: Isolation of P1 and P2 Bis(carbene) Adducts. *Angew. Chem., Int. Ed.* **2009**, *48*, 5530–5533.
19. Loss, S.; Magistrato, A.; Cataldo, L.; Hoffmann, S.; Geoffroy, M.; Röthlisberger, U.; Grützmacher, H. Isolation of a Highly Persistent Diphosphanyl Radical: the Phosphorus Analogue of a Hydrazyl. *Angew. Chem., Int. Ed.* **2001**, *40*, 723–726.
20. Stevenson, D. P.; Yost, D. M. The Thermodynamic Properties of Phosphorus, Phosphine, and Some Phosphorus Halides. *J. Chem. Phys.* **1941**, *9*, 403–408.
21. Buscema, M.; Groenendijk, D. J.; Blanter, S. I.; Steele, G. A.; van der Zant, H. S. J.; Castellanos-Gomez, A. Fast and Broadband Photoresponse of Few-Layer Black Phosphorus Field-Effect Transistors. *Nano Lett.* **2014**, *14*, 3347–3352.
22. Deng, Y.; Conrad, N. J.; Luo, Z.; Liu, H.; Xu, X.; Ye, P. D. Towards High-Performance Two-Dimensional Black Phosphorus Optoelectronic Devices: the Role of Metal Contacts. *IEEE IEDM* **2014**, 5.2.1–5.2.4.
23. Sang, L.; Liao, M.; Sumiya, M. A Comprehensive Review of Semiconductor Ultraviolet Photodetectors: From Thin Film to One-Dimensional Nanostructures. *Sensors* **2013**, *13*, 10482–10518.
24. Sugai, S.; Shirotani, I. Raman and Infrared Reflection Spectroscopy in Black Phosphorus. *Solid State Commun.* **1985**, *53*, 753–755.
25. Schroder, D. K. *Semiconductor Material and Device Characterization*; John Wiley & Sons: New York, 2006.
26. Lin, J. D.; Han, C.; Wang, F.; Wang, R.; Xiang, D.; Qin, S.; Zhang, X.-A.; Wang, L.; Zhang, H.; Wee, A. T. S.; et al. Electron-Doping-Enhanced Trion Formation in Monolayer Molybdenum Disulfide Functionalized with Cesium Carbonate. *ACS Nano* **2014**, *8*, 5323–5329.
27. Xiang, D.; Han, C.; Zhang, J.; Chen, W. Gap States Assisted MoO_3 Nanobelt Photodetector with Wide Spectrum Response. *Sci. Rep.* **2014**, *4*, 4891.
28. Hu, L.; Yan, J.; Liao, M.; Wu, L.; Fang, X. Ultrahigh External Quantum Efficiency from Thin SnO_2 Nanowire Ultraviolet Photodetectors. *Small* **2011**, *7*, 1012–1017.
29. Soci, C.; Zhang, A.; Xiang, B.; Dayeh, S. A.; Aplin, D. P. R.; Park, J.; Bao, X. Y.; Lo, Y. H.; Wang, D. ZnO Nanowire UV Photodetectors with High Internal Gain. *Nano Lett.* **2007**, *7*, 1003–1009.
30. Zhang, W.; Chuu, C.-P.; Huang, J.-K.; Chen, C.-H.; Tsai, M.-L.; Chang, Y.-H.; Liang, C.-T.; Chen, Y.-Z.; Chueh, Y.-L.; He, J.-H.; et al. Ultrahigh-Gain Photodetectors Based on Atomically Thin Graphene-MoS_2 Heterostructures. *Sci. Rep.* **2014**, *4*, 3826.
31. Konstantatos, G.; Sargent, E. H. Nanostructured Materials for Photon Detection. *Nat. Nanotechnol.* **2010**, *5*, 391–400.
32. Konstantatos, G.; Badioli, M.; Gaudreau, L.; Osmond, J.; Bernechea, M.; de Arquer, F. P. G.; Gatti, F.; Koppens, F. H. L. Hybrid Graphene-Quantum Dot Phototransistors with Ultrahigh Gain. *Nat. Nanotechnol.* **2012**, *7*, 363–368.
33. Konstantatos, G.; Levina, L.; Fischer, A.; Sargent, E. H. Engineering the Temporal Response of Photoconductive Photodetectors *via* Selective Introduction of Surface Trap States. *Nano Lett.* **2008**, *8*, 1446–1450.
34. Manga, K. K.; Wang, J.; Lin, M.; Zhang, J.; Nesladek, M.; Nalla, V.; Ji, W.; Loh, K. P. High-Performance Broadband Photodetector Using Solution-Processible PbSe−TiO_2−Graphene Hybrids. *Adv. Mater.* **2012**, *24*, 1697–1702.
35. Carvalho, A.; Ribeiro, R.; Castro Neto, A. Band Nesting and the Optical Response of Two-Dimensional Semiconducting Transition Metal Dichalcogenides. *Phys. Rev. B: Condens. Matter Mater. Phys.* **2013**, *88*, 115205.

36. Yuan, H.; Liu, X.; Afshinmanesh, F.; Li, W.; Xu, G.; Sun, J.; Lian, B.; Ye, G.; Hikita, Y.; Shen, Z. Broadband Linear-Dichroic Photodetector in a Black Phosphorus Vertical pn Junction. *arXiv preprint arXiv:1409.4729* **2014**.
37. Ziletti, A.; Carvalho, A.; Campbell, D.; Coker, D.; Neto, A. Oxygen Defects in Phosphorene. *arXiv preprint arXiv:1407.5880* **2014**.
38. Avsar, A.; Vera-Marun, I. J.; Tan, J. Y.; Watanabe, K.; Taniguchi, T.; Castro Neto, A. H.; Özyilmaz, B. Air-Stable Transport in Graphene-Contacted, Fully Encapsulated Ultrathin Black Phosphorus-Based Field-Efect Transistors. *ACS Nano* **2015**, *9*, 4138–4145.
39. Liu, H.; Neal, A. T.; Ye, P. D. In *Ambipolar Phosphorene Field-Effect Transistors with Dielectric Capping*; 72nd Annual Device Research Conference (DRC); IEEE: Hoboken, 2014; 201−202.
40. Zhang, W. J.; Chuu, C. P.; Huang, J. K.; Chen, C. H.; Tsai, M. L.; Chang, Y. H.; Liang, C. T.; Chen, Y. Z.; Chueh, Y. L.; He, J. H.; et al. Ultrahigh-Gain Photodetectors Based on Atomically Thin Graphene-MoS_2 Heterostructures. *Sci. Rep.* **2014**, *4*, 3826.
41. Roy, K.; Padmanabhan, M.; Goswami, S.; Sai, T. P.; Ramalingam, G.; Raghavan, S.; Ghosh, A. Graphene-MoS_2 Hybrid Structures for Multifuntional Photoresponsive Memory Devices. *Nat. Nanotechnol.* **2013**, *8*, 826–830.
42. Skuja, L.; Hirano, M.; Hosono, H.; Kajihara, K. Defects in Oxide Glasses. *Phys. Status Solidi C* **2005**, *2*, 15–24.
43. Schwidtal, K. SiO_2 Surface Defect Centers Studied by AES. *Surf. Sci.* **1978**, *77*, 523–536.
44. Castellanos-Gomez, A.; Vicarelli, L.; Prada, E.; Island, J. O.; Narasimha-Acharya, K.; Blanter, S. I.; Groenendijk, D. J.; Buscema, M.; Steele, G. A.; Alvarez, J. Isolation and Characterization of Few-Layer Black Phosphorus. *arXiv preprint arXiv:1403.0499*, **2014**.
45. Giannozzi, P.; Baroni, S.; Bonini, N.; Calandra, M.; Car, R.; Cavazzoni, C.; Ceresoli, D.; Chiarotti, G. L.; Cococcioni, M.; Dabo, I. QUANTUM ESPRESSO: a Modular and Open-Source Software Project for Quantum Simulations of Materials. *J. Phys.: Cond. Mater.* **2009**, *21*, 395502.
46. Blöchl, P. Projector Augmented-Wave Method. *Phys. Rev. B: Condens. Matter Mater. Phys.* **1994**, *50*, 17953–17979.
47. Perdew, J.; Ruzsinszky, A.; Csonka, G.; Vydrov, O.; Scuseria, G.; Constantin, L.; Zhou, X.; Burke, K. Restoring the Density-Gradient Expansion for Exchange in Solids and Surfaces. *Phys. Rev. Lett.* **2008**, *100*, 136406.
48. Perdew, J.; Burke, K.; Ernzerhof, M. Generalized Gradient Approximation Made Simple. *Phys. Rev. Lett.* **1996**, *77*, 3865–3868.
49. Monkhorst, H.; Pack, J. Special Points for Brillouin-Zone Integrations. *Phys. Rev. B* **1976**, *13*, 5188–5192.
50. Umari, P.; Pasquarello, A.; Dal Corso, A. Raman Scattering Intensities in α-Quartz: A First-Principles Investigation. *Phys. Rev. B: Condens. Matter Mater. Phys.* **2001**, *63*, 094305.